

# Sodium Ion Stabilized Vanadium Oxide Nanowire Cathode for High-Performance Zinc-Ion Batteries

Pan He, Guobin Zhang, Xiaobin Liao, Mengyu Yan,\* Xu Xu, Qinyou An, Jun Liu, and Liqiang Mai\*

Aqueous Zn-ion batteries (ZIBs) have received incremental attention because of their cost-effectiveness and the materials abundance. They are a promising choice for large-scale energy storage applications. However, developing suitable cathode materials for ZIBs remains a great challenge. In this work, pioneering work on the designing and construction of aqueous Zn//Na<sub>0.33</sub>V<sub>2</sub>O<sub>5</sub> batteries is reported. The Na<sub>0.33</sub>V<sub>2</sub>O<sub>5</sub> (NVO) electrode delivers a high capacity of 367.1 mA h g<sup>-1</sup> at 0.1 A g<sup>-1</sup>, and exhibits long-term cyclic stability with a capacity retention over 93% for 1000 cycles. The improvement of electrical conductivity, resulting from the intercalation of sodium ions between the [V<sub>4</sub>O<sub>12</sub>]<sub>n</sub> layers, is demonstrated by single nanowire device. Furthermore, the reversible intercalation reaction mechanism is confirmed by X-ray diffraction, Raman, X-ray photoelectron spectroscopy, scanning electron microscopy, and transmission electron microscopy analysis. The outstanding performance can be attributed to the stable layered structure and high conductivity of NVO. This work also indicates that layered structural materials show great potential as the cathode of ZIBs, and the indigenous ions can act as pillars to stabilize the layered structure, thereby ensuring an enhanced cycling stability.

The clean energy resources such as the solar and wind power are promoted vigorously caused by the continuous increase of energy crisis and environmental pollution.<sup>[1–3]</sup> Thus, there has been a growing requirement for large-scale energy storage devices.<sup>[4,5]</sup> Currently, lithium-ion batteries (LIBs) and sodium-ion batteries (SIBs) are considered as the most promising energy storage devices due to their higher energy density compared to

other secondary batteries.<sup>[6–8]</sup> However, LIBs are too expensive to scale up for the processing cost resulted from the limited lithium resources, and SIBs are subjected to complicated issues of safety as well as environmental issues.<sup>[9–12]</sup> So, it is an urgent challenge for exploring new energy storage systems. As an alternative, rechargeable aqueous Zn-ion batteries (ZIBs) have received incremental attention owing to the following advantages, including low cost, safety, and environmentally friendly.<sup>[13]</sup> Meanwhile, using aqueous electrolyte to replace the organic electrolyte is of great significance for reducing the cost and environmental pollution.<sup>[14]</sup> However, it is difficult to find suitable cathode material as the host for the intercalation of Zn<sup>2+</sup> owing to the high polarization of Zn<sup>2+</sup> as well as the narrow applicable voltage range, which is limited by the water splitting in the aqueous battery system.<sup>[15]</sup>

Typically, polymorphs of MnO<sub>2</sub> ( $\alpha$ ,  $\gamma$  phase) are highly attractive as the cathode material because of the tunnel structure suiting for the intercalation of Zn<sup>2+</sup> and a matched potential within the stable range of water. Some results, based on the reversible intercalation of Zn<sup>2+</sup>, have been reported in recent years, and they show either limited specific capacity or poor cycling performance.<sup>[16–19]</sup> Recently, the MnO<sub>2</sub> nanofiber electrode, reported by Liu and co-workers, shows high capacity and excellent cycling performance.<sup>[20]</sup> However, the rate performance is not high enough due to the sluggish reaction dynamics of conversion reaction. Prussian blue analogues, including of zinc hexacyanoferrate and copper hexacyanoferrate, are another class of cathode materials, which show limited specific capacity as well as poor cyclic stability.<sup>[21–23]</sup> Until very recently, vanadium-based materials are explored for reversible Zn<sup>2+</sup> intercalation.<sup>[24]</sup> Nazar and co-workers reported a bilayered Zn<sub>0.25</sub>V<sub>2</sub>O<sub>5</sub>·nH<sub>2</sub>O cathode, which shows a high-capacity and long-life performance.<sup>[25]</sup> However, the development of ZIBs is in the primary stage, some new cathode materials should also be explored to enhance the energy density as well as cycle life for ZIBs.

Over the past decades, layered vanadium oxides have been applied as electrode materials for LIBs or SIBs due to their low cost and high capacities.<sup>[26,27]</sup> Generally, the bulk vanadium oxides suffer from a rapid capacity fading resulting from low electronic conductivity, poor structural stability during the ion de/intercalation.<sup>[28]</sup> Recent studies show that interlayer metal ions (M<sub>x</sub>V<sub>n</sub>O<sub>m</sub>, M = metal ion) can act as pillars to increase the

Dr. P. He, Dr. G. Zhang, Dr. X. Liao, Dr. M. Yan, Dr. X. Xu, Prof. Q. An, Prof. J. Liu, Prof. L. Mai  
State Key Laboratory of Advanced Technology for Materials Synthesis and Processing  
International School of Materials Science and Engineering  
Wuhan University of Technology  
Wuhan 430070, P. R. China  
E-mail: ymymiles@whut.edu.cn; mlq518@whut.edu.cn

Dr. M. Yan  
Department of Materials Science and Engineering  
University of Washington  
Seattle, WA 98195-2120, USA

Prof. L. Mai  
Department of Chemistry  
University of California  
Berkeley, CA 94720, USA

 The ORCID identification number(s) for the author(s) of this article can be found under <https://doi.org/10.1002/aenm.201702463>.

DOI: 10.1002/aenm.201702463

stability of layered vanadium oxides.<sup>[29,30]</sup> The ion diffusion rate, as well as the electronic conductivity, can be greatly improved by the interlayer metal ions of these host vanadium oxides. However, only a few studies focus on the effect of interlayer metal ions in the system of ZIBs. Herein, we present a low-cost, safe, high capacity (367.1 mA h g<sup>-1</sup> at a current density of 0.1 A g<sup>-1</sup>) and long life (with the capacity retention over 93% for 1000 cycles) aqueous ZIBs, which comprises of Na<sub>0.33</sub>V<sub>2</sub>O<sub>5</sub> (NVO) nanowire cathode, 3 M Zn(CH<sub>3</sub>F<sub>3</sub>SO<sub>3</sub>)<sub>2</sub> electrolyte, and a zinc anode. During electrochemical processes, the morphological and structural evolution of NVO nanowire cathode are studied by field emission scanning electron microscopy (FESEM), X-ray photoelectron spectroscopy (XPS), transmission electron microscopy (TEM) as well as X-ray diffraction (XRD). Moreover, the effects of interlayer Na<sup>+</sup> are investigated by assembling single nanowire device, which provides a direct evidence for the improved electrical conductivity in layered vanadium oxide.

There are three different vanadium sites named V(1), V(2), and V(3) in NVO crystal structure (Figure S1, Supporting Information). The V(1)O<sub>6</sub> octahedra form zigzag chains and the V(2)O<sub>6</sub> octahedra form double chains along the *b* axis, respectively. The [V<sub>4</sub>O<sub>12</sub>]<sub>n</sub> layer, consisting of these two units, are further linked by oxygen atoms to form 2D [V<sub>4</sub>O<sub>12</sub>]<sub>n</sub> layered structure along the (001) plane with Na<sup>+</sup> intercalating between the layers. The [V<sub>4</sub>O<sub>12</sub>]<sub>n</sub> layers are connected by V(3)O<sub>5</sub> and edge-sharing oxygen atoms, forming a 3D tunnel structure. The intercalating Na<sup>+</sup> between the [V<sub>4</sub>O<sub>12</sub>]<sub>n</sub> layers can act as “pillars” to increase the 3D stability of the tunnel structure upon ions insertion/extraction (the inset in Figure 1a). The XRD pattern of the as-prepared NVO product is shown in Figure 1a. All the

diffraction peaks of the pattern can be well-indexed to a pure monoclinic Na<sub>0.33</sub>V<sub>2</sub>O<sub>5</sub> phase (JCPDS no. 86-0120, *a* = 10.0880 Å, *b* = 3.6170 Å, *c* = 15.4490 Å) and no obvious impurity peaks are detected. By contrast, the XRD pattern of V<sub>2</sub>O<sub>5</sub> can be indexed to a pure orthorhombic phase (JCPDS no. 41-1426) (Figure S2, Supporting Information). The Raman spectrum of the NVO in the range of 100–1100 cm<sup>-1</sup> is shown in Figure 1b. Six obvious peaks located at 144.5, 197.6, 284.1, 410.3, 697.7, and 1013.8 cm<sup>-1</sup> are observed, which can be assigned to the stretching vibrations of particular V–O bonds in the (V1)O<sub>6</sub>, (V2)O<sub>6</sub>, and (V3)O<sub>5</sub> polyhedra.<sup>[31]</sup> The Raman band at 410 cm<sup>-1</sup> originates from the stretching of V2–O5 and the bending of V1–O5–V3, the 697 cm<sup>-1</sup> mode corresponds to the antisymmetric stretching of V1–O2–V1 and the mode at 1013 cm<sup>-1</sup> represents the V2–O6 stretching vibration.<sup>[32]</sup>

The morphology and microstructures of the as-prepared NVO and V<sub>2</sub>O<sub>5</sub> are investigated by FESEM, TEM, and energy dispersive X-ray (EDX) element mapping. The FESEM images show that the NVO sample consists of a mass of nanowire with an average diameter of 50–200 nm (Figure 1c; Figure S3, Supporting Information). Note that the as-prepared V<sub>2</sub>O<sub>5</sub> shows a similar morphology to that of NVO sample (Figure S4, Supporting Information). Both NVO and V<sub>2</sub>O<sub>5</sub> nanowire show smooth and clean surface. TEM investigations are carried out to further study the morphology and structure of the NVO sample. The NVO TEM image shows a wire-like morphology with a diameter about 100 nm (Figure 1d). The HRTEM image of the individual nanowire shows the clearly resolved lattice fringe with a spacing of 0.501 nm, corresponding to the (102) planes of NVO (Figure 1e). The selected area electron

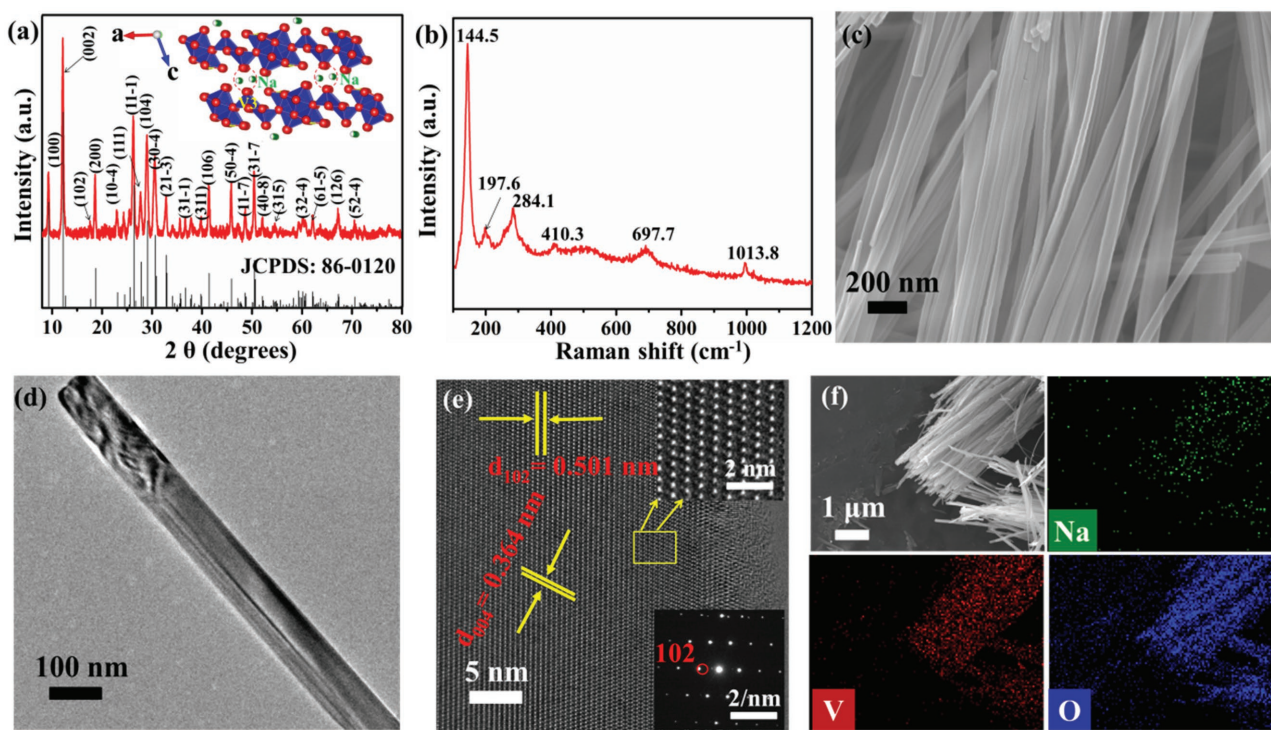


**Figure 1.** a) XRD pattern and the insets show the crystal structure of NVO nanowire. b) Raman spectra, c) FESEM image, d) TEM image, e) high resolution TEM image, the inset shows the SAED pattern and f) SEM-EDX element mapping images of NVO nanowire.

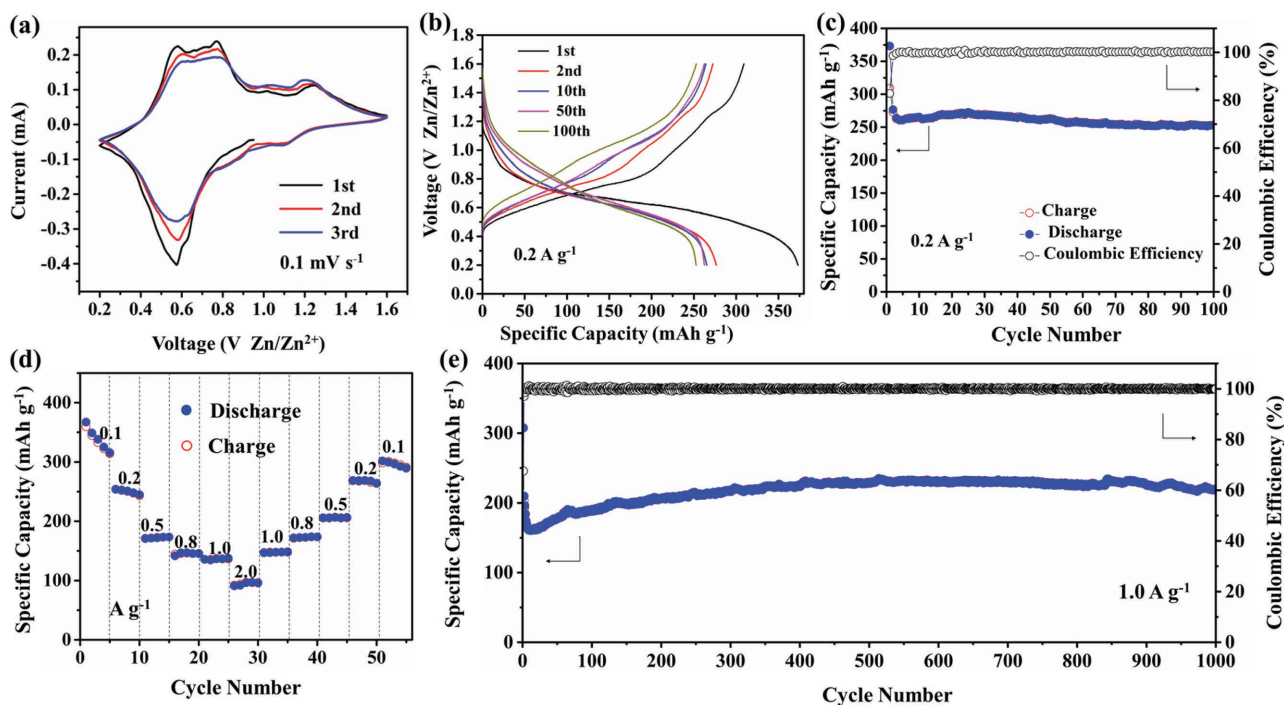


**Figure 2.** a) The CV curves of NVO electrode at a scan rate of  $0.1 \text{ mV s}^{-1}$  in the voltage range of 0.2–1.6 V. b) The galvanostatic charge/discharge curves of NVO at  $0.2 \text{ A g}^{-1}$ . c) Cycling performance of NVO at  $0.2 \text{ A g}^{-1}$ . d) Rate performance of NVO. e) Cycling performance of NVO at  $1.0 \text{ A g}^{-1}$ .

diffraction (SAED) image (the inset in Figure 1e) indicates its single crystalline nature and a monoclinic pattern, which corresponds to the XRD result. The elemental mapping is applied to determine the distribution of the element of Na, V, and O (Figure 1f). The result clearly indicates that Na, V, and O element are uniformly distributed with no other element detected.

The electrochemical performances of NVO and  $\text{V}_2\text{O}_5$  as the cathode materials and the zinc metal as the counter electrode for ZIBs are investigated in detail. **Figure 2a** displays the cyclic voltammogram (CV) of NVO at a scan rate of  $0.1 \text{ mV s}^{-1}$  with  $3 \text{ M Zn}(\text{CH}_3\text{F}_3\text{SO}_3)_2$  electrolyte in a voltage range of 0.2–1.6 V (vs  $\text{Zn}^{2+}/\text{Zn}$ ). There are four pairs of cathodic/anodic peaks, located at 1.25/1.10, 1.02/0.79, 0.77/0.63, and 0.58/0.52 V. In order to understand those cathodic and anodic peaks, the CV curve of NVO at a scan rate of  $0.2 \text{ mV s}^{-1}$  in a voltage range of 1.5–4.0 V (vs  $\text{Li}^+/\text{Li}$ ) is studied (Figure S5, Supporting Information). In the voltage range of 2.2–4.0 V, there are four redox peaks of NVO electrode, located at 3.52/3.36, 3.31/3.26, 2.98/2.87, and 2.88/2.48 V. These redox peaks can be ascribed to the multistep  $\text{Li}^+$  de/intercalation behaviors in NVO.<sup>[33]</sup> Generally, the potential of  $\text{Zn}^{2+}/\text{Zn}$  is 2.26 V higher than the potential of  $\text{Li}^+/\text{Li}$ . Thus, the four pairs of peaks (1.25/1.10, 1.02/0.79, 0.77/0.63, and 0.58/0.52 V) could be ascribed to the multistep  $\text{Zn}^{2+}$  de/intercalation behaviors in NVO. The galvanostatic charge and discharge curves of NVO at different cycles at the current density of  $0.2 \text{ A g}^{-1}$  in the voltage range of 0.2–1.6 V are shown in Figure 2b. All the charge/discharge voltage plateaus connect together to form a long and tilting platform. The first discharge curve shows greatly different from the subsequent, corresponding well with the first CV curve. From the 2nd to 100th cycle, all the discharge curves show similar shape, which indicates a high reversibility

of charge/discharge process. The cyclic performance of NVO electrode at a current density of  $0.2 \text{ A g}^{-1}$  is further investigated as shown in Figure 2c. The specific discharge capacity of the first cycle is  $373.2 \text{ mA h g}^{-1}$ , which is much higher than the second cycle ( $276.6 \text{ mA h g}^{-1}$ ). The reason is that the inserted Zn ions, located at the “dead  $\text{Zn}^{2+}$  sites,” cannot be extracted from the NVO lattice during the following charge process. The similar phenomenon can be found when other vanadium oxide materials as cathodes for ZIBs, such as  $\text{LiV}_3\text{O}_8$  and  $\text{V}_2\text{O}_5$ .<sup>[34,35]</sup> An outstanding capacity retention ratio of 91.3% (against the second cycle) is available after 100 cycles and the coulombic efficiency approaches to 100% in all cycles. Rate performance of NVO and  $\text{V}_2\text{O}_5$  electrode are measured as shown in Figure 2d and Figure S6 (Supporting Information). The discharge capacities of NVO are 367.1, 253.7, 173.4, 145.3, 137.5, and  $96.4 \text{ mA h g}^{-1}$  at current densities of 0.1, 0.2, 0.5, 0.8, 1.0, and  $2.0 \text{ A g}^{-1}$ , respectively. The NVO electrode exhibits a good cycling performance at various current rates while the  $\text{V}_2\text{O}_5$  electrode exhibits unstable specific capacities at initial few cycles and suffers a rapid capacity fading at increased current densities. Additionally, the NVO electrode also exhibits an outstanding cycling stability, maintaining a discharge capacity of  $218.4 \text{ mA h g}^{-1}$ , with a capacity retention over 93% (against the highest capacities of 2–1000th) at a high current density of  $1.0 \text{ A g}^{-1}$  after 1000 cycles (Figure 2e, corresponding galvanostatic charge and discharge curves are shown in Figure S7a of the Supporting Information). However, the  $\text{V}_2\text{O}_5$  electrode shows a poor cycling stability, maintaining a relatively low discharge capacity of  $52.9 \text{ mA h g}^{-1}$ , after 680 cycles at the current density of  $1.0 \text{ A g}^{-1}$  (Figure S8, Supporting Information). Interestingly, there are obvious increasing of the capacities for both NVO and  $\text{V}_2\text{O}_5$  in the initial

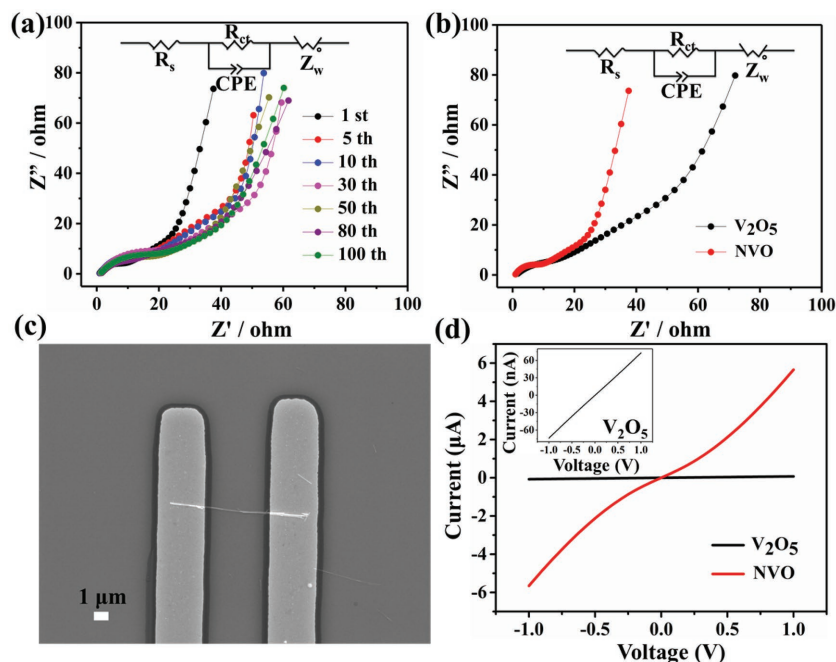


**Figure 3.** a) Alternating-current impedance plots of NVO after different cycles. b) Alternating-current impedance plots of NVO and  $V_2O_5$  after the 1st cycle. c) SEM image of the NVO single nanowire device. d) The  $I$ - $V$  curves of NVO and  $V_2O_5$ .

stage, which are attributed to the gradual activation of the electrode and similar tendency is reported in previous work about vanadate.<sup>[33]</sup> The CV curves of NVO and  $V_2O_5$  electrode at a scan rate of  $0.5 \text{ mV s}^{-1}$  are shown in Figure S9 (Supporting Information). The capacity of NVO decreases with cycling in the initial ten cycles and gradually increases in the following cycles, which is consistent with the cycling performance at  $1.0 \text{ A g}^{-1}$ . However, the jagged jitter and increasing polarization appears in the CV curves of  $V_2O_5$  after 10 cycles and similar phenomena are observed in the galvanostatic charge/discharge curves of  $V_2O_5$  electrode, related to the structure degradation and conductivity decline, which is the intrinsic factors for capacity fading (Figures S6b and S7b, Supporting Information).<sup>[36]</sup>

Electrochemical impedance spectroscopy (EIS) measurements are carried out on the Zn//NVO and Zn// $V_2O_5$  battery to understand the detailed reaction kinetics of the electrode materials. Generally, in the equivalent circuit (inset of Figure 3a,b),  $R_s$  stands for all equivalent series resistance while  $R_{ct}$  represents the charge transfer resistance between the electrode/electrolyte interface and the contacts with electrode materials.<sup>[37]</sup> The initial  $R_{ct}$  is  $15.0 \Omega$  and it decreases to nearly a third of the original state after the first cycle ( $5.6 \Omega$  after the first cycle). The spectra of NVO electrode at different cycles are collected as shown in Figure 3a. The  $R_{ct}$  increases during the former 30 cycles, and the  $R_{ct}$  of different cycles (1st, 5th, 30th, 50th, 80th, and 100th) are 5.6, 10.0, 11.5, 16.1, 13.8, 11.2, and  $13.0 \Omega$ , respectively (Table S1, Supporting Information). Meanwhile, the EIS spectrum of  $V_2O_5$  electrode after the first cycle is shown in Figure 3b and Table S2 (Supporting Information). The  $R_{ct}$  of  $V_2O_5$  electrode is  $8.7 \Omega$ , which is 1.5 times larger than the charge transfer resistance of NVO electrode. In order to further verify the results above, the NVO and  $V_2O_5$  single nanowire devices

are designed and assembled as shown in Figure 3c and Figure S11 (Supporting Information). The conductivity of NVO and  $V_2O_5$  single nanowires are tested by choosing a specific nanowire, which can avoid the influence of conductive additives and binders during the battery assembling process. Through calculation and analysis, the conductivity of  $V_2O_5$  is  $7.3 \text{ S m}^{-1}$ , while the conductivity of NVO is  $5.9 \times 10^4 \text{ S m}^{-1}$ , which indicates that electronic conductivity of  $V_2O_5$  is greatly improved by the intercalation of sodium ions.

To clearly reveal the storage mechanism of Zn//NVO system, the structural, valence states, and morphology evolutions of NVO nanowires are characterized by XRD, XPS, FESEM, and TEM after zinc-ion insertion and extraction process. Figure 4a displays the XRD pattern of NVO electrode at the third cycle (corresponding charge–discharge curve is shown in Figure 4b) at the current density of  $0.2 \text{ A g}^{-1}$ . The four major peaks, located at  $9.3^\circ$ ,  $12.2^\circ$ ,  $18.7^\circ$ , and  $29.0^\circ$ , shift repeatedly during the galvanostatic discharge and charge processes, which reflect the variation of (100), (002), (200), and (104), respectively. A new phase is observed during the discharge process,

as illustrated in Figure 4c. In the voltage range of  $0.7$ – $1.6 \text{ V}$ , there is only a small change of the XRD patterns, indicating a slight change of the interlayer distance in low zinc content ( $Zn_xNa_{0.33}V_2O_5$ ,  $0 < x < 0.42$ ). Interestingly, three peaks, located at  $6.6^\circ$ ,  $13.2^\circ$ , and  $19.7^\circ$ , sharply appear and gradually strength when discharging from  $0.7$  to  $0.2 \text{ V}$  (corresponding to the zinc content of  $0.42 < x < 0.96$ ), which is attributed to the forming/disappearing of the new phase ( $Zn_xNa_{0.33}V_2O_5$ ), resulting from the increase of the  $Zn^{2+}$  content. In contrast, these three peaks gradually weaken and disappear during the charge progress. To further explain the phase transform process, in situ XRD patterns are collected as shown in Figure S12 (Supporting Information). A reversible phase transform between  $Na_{0.33}V_2O_5$  and the new phase is observed during the charge/discharge process. Also, not all the initial phase ( $Na_{0.33}V_2O_5$ ) is converted to the intercalated phase, which is in accord with the ex situ XRD result (Figure 4a). The intensity and position evolution of the selected peaks, located at  $29.0^\circ$  and  $41.3^\circ$ , shift to lower angles after fully discharge process, clearly show that the structure continues to evolve upon  $Zn^{2+}$  insertion. Based on the Rietveld refinement results of different charged/discharged state, the new peaks can be indexed to the inserted  $Zn_xNa_{0.33}V_2O_5$  phase, and the structural change of NVO is a highly reversible process (Figure S13, Supporting Information). The Raman spectrum of NVO samples at different charge/discharge states are shown in Figure S14 (Supporting Information). The highest peak located at  $144.5 \text{ cm}^{-1}$ , which is tightly coupled with the layered structure, becoming weaker and broader when the NVO electrode is discharging to  $0.2 \text{ V}$ , and gradually returning to the original state when it is recharging to  $1.6 \text{ V}$ , indicating a stable layered structure. The ex situ XPS analysis (Figure S15, Supporting Information) of NVO electrodes in original and discharged

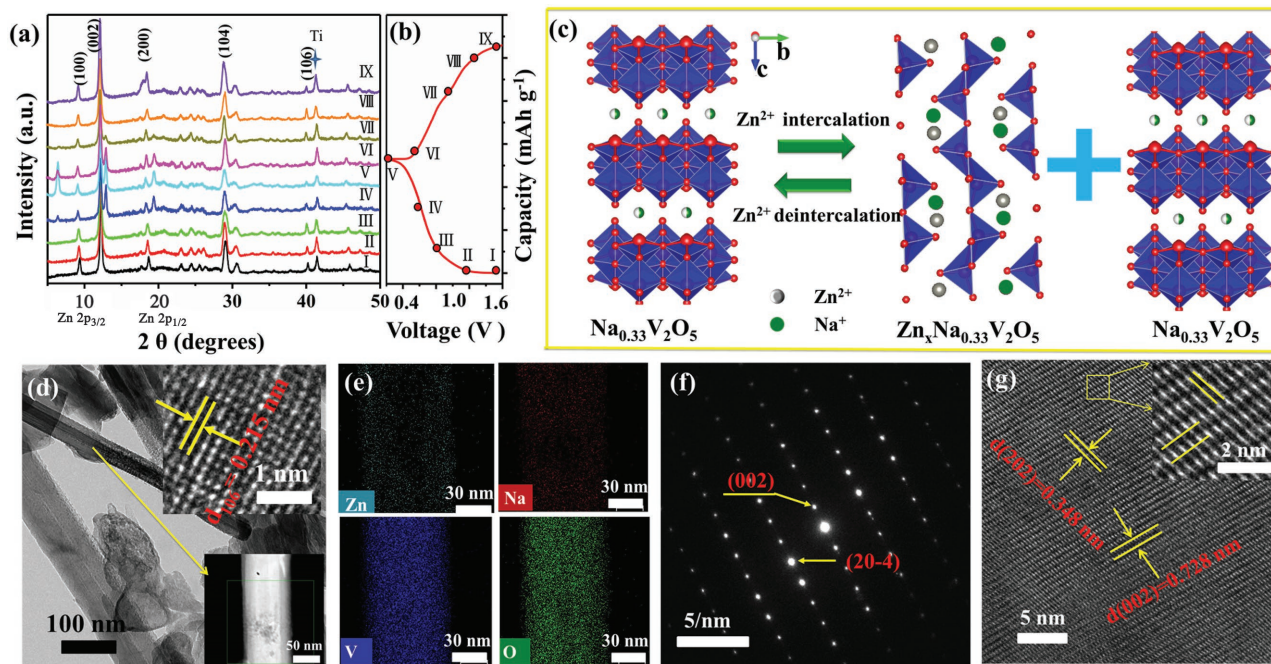


**Figure 4.** a) The ex situ XRD patterns of NVO electrode at different charge/discharge states, and b) corresponding galvanostatic charge and discharge curves at  $0.2 \text{ A g}^{-1}$ . c) Schematic illustration of the zinc-storage mechanism in the NVO electrode. d) TEM and e) TEM-EDX element mapping images at a full discharge state of NVO electrode after 3 cycles. f) The SAED pattern and g) HRTEM image of NVO electrode after 100 cycles.

(at the potential of  $0.2 \text{ V}$ ) states are further applied to verify the result of XRD. The survey spectrum indicates that the sample consists of Na, V, O, and C (the addition of acetylene black) elements in original state, while Zn 2p core level spectra appeared at discharged state. High resolution spectra in the range of  $512\text{--}526 \text{ eV}$  and  $1018\text{--}1052 \text{ eV}$  are recorded to further understand the valence states of V (Figure S15b, Supporting Information) and the intensity of zinc (Figure S15c, Supporting Information), respectively. Two peaks located at  $514.8$  and  $516.5 \text{ eV}$  are observed in the range of  $512\text{--}520 \text{ eV}$ , corresponding to the binding energy of  $\text{V}^{4+}$  and  $\text{V}^{5+}$  ( $\text{V } 2p_{3/2}$  band), respectively.<sup>[38]</sup> Similarly, two different peaks located at  $523.3$  and  $524.7 \text{ eV}$  are observed in the range of  $520\text{--}526 \text{ eV}$ , corresponding to the binding energy of V  $2p_{1/2}$  band. Note that the peak area ratio of  $\text{V}^{4+}$  and  $\text{V}^{5+}$  changes greatly from the original to the discharged state. The  $\text{V}^{4+}$  signal intensifies strongly upon discharge (a small amount of  $\text{V}^{3+}$  component is included in the broad peak of  $\text{V}^{4+}$ ), which is in accord with the reduction to an average valence of  $\text{V}^{3.87+}$  based on the electrochemistry. Furthermore, the intensity of Zn 2p of the original state is far below that of discharged state, which confirmed the insertion of  $\text{Zn}^{2+}$  into the NVO electrode. TEM and TEM-EDX element mapping images at a full discharge state of NVO electrode after 3 cycles are collected (Figure 4d,e). The morphology of NVO nanowire is well maintained and the HRTEM image (inset in Figure 4d) shows a clear lattice fringe, indicating a high stable crystallinity. The elements of Zn, Na, V, and O are uniformly distributed as shown in TEM-EDX element mapping images (Figure 4e; Figure S16, Supporting Information). Combining with the XRD, Raman, XPS, and TEM results, the storage mechanism of Zn//NVO battery can be well illustrated. A reversible zinc ions insertion/extraction in/out the NVO material can be confirmed from all aspects.

To confirm the NVO active material in the subsequent cycles, TEM images of the electrode at full charge state after 100 cycles are collected (Figure 4f,g; Figure S17, Supporting Information). The TEM image shows that the NVO material still maintains nanowire morphology. Similar results are obtained by the SEM images of NVO nanowire after 3rd, 100th, 1000th, 2000th cycle (Figure S18, Supporting Information). The morphology of NVO nanowire is well maintained after 1000 cycles, even after 2000 cycles with little cracks. However, the morphology of  $\text{V}_2\text{O}_5$  suffers great damage, with many cracks of the nanowires (Figure S19, Supporting Information). The SAED pattern confirms the single crystalline of NVO (Figure 4f), and the HRTEM image shows a clear lattice fringe with a spacing of  $0.728 \text{ nm}$ , corresponding to the (002) planes of NVO (Figure 4g). In addition, the inductively coupled plasma optical emission spectroscopy analysis (ICP-OES) of the electrolyte after different cycles is tested through a three-electrode measurement (Table S3, Supporting Information). The result shows that only little variety of the amount of vanadium and sodium elements are captured in the electrolyte, indicating little dissolution ( $<1\%$  of the active material) of the active material. The result of the ICP-OES analysis of the electrodes at different states show that the sodium content is stable at different states (Table S4, Supporting Information), which is in accordance with the previous ICP-result of the electrolyte. In other words, the sodium ion does not change during charge/discharge process, and it cannot be extracted from NVO during the charge process. Also, the XRD patterns of NVO at different cycles show no obvious change after 200 cycles, indicating that the 3D tunnel framework of NVO is maintained by the  $\text{Na}^+$  between the  $[\text{V}_4\text{O}_{12}]_n$  layers, which acts as “pillars” to maintain the structural stability during the charge/discharge progress (Figure S20, Supporting Information). However, the XRD pattern of  $\text{V}_2\text{O}_5$  after 100 cycles

is different from the initial (Figure S21, Supporting Information). The peak located at 20.3° shifts to 21.2°, corresponding to a decrease of (001) crystalline spacing, which results from the structure degradation. Together with the SEM and TEM results, it can be concluded that the 3D tunnel structure of NVO are well maintained during the charge/discharge progress, which owes to the stable Na<sup>+</sup> between the [V<sub>4</sub>O<sub>12</sub>]<sub>n</sub> layers.

In summary, aqueous Zn//NVO battery is designed and constructed for the first time, which comprises of NVO nanowire cathode, 3 M Zn(CH<sub>3</sub>F<sub>3</sub>SO<sub>3</sub>)<sub>2</sub> electrolyte and a zinc anode. The NVO electrode delivers a high capacity (367.1 mA h g<sup>-1</sup> at 0.1 A g<sup>-1</sup>), exhibits long-term cyclic stability (with a capacity retention over 93% for 1000 cycles) and good rate performance. The improvement of electrical conductivity, resulted from the intercalation of sodium ions between the [V<sub>4</sub>O<sub>12</sub>]<sub>n</sub> layers, is studied by single nanowire device. Furthermore, the reversible intercalation reaction mechanism is also confirmed by XRD, Raman, XPS, SEM, and TEM analysis. The outstanding performances can be attributed to the stable layered structure and high conductivity of NVO. This work also indicates that layered structure materials show great potential for the cathode of ZIBs and the indigenous ions can act as pillars to stabilize the layered structure, thereby ensuring an enhanced cycling stability.

## Supporting Information

Supporting Information is available from the Wiley Online Library or from the author.

## Acknowledgements

This work was supported by the National Key Research and Development Program of China (2016YFA0202603), the National Basic Research Program of China (2013CB934103), the Programme of Introducing Talents of Discipline to Universities (B17034), the National Natural Science Foundation of China (51521001, 51602239), the National Natural Science Fund for Distinguished Young Scholars (51425204), the Hubei Provincial Natural Science Foundation of China (2016CFB267), and the Fundamental Research Funds for the Central Universities (WUT: 2016111001, 2016111003, 20161VA090). L.M. gratefully acknowledged financial support from China Scholarship Council (No. 201606955096).

## Conflict of Interest

The authors declare no conflict of interest.

## Keywords

intercalation, large-scale energy storage, Zn ion batteries, Zn//Na<sub>0.33</sub>V<sub>2</sub>O<sub>5</sub>

Received: September 6, 2017

Revised: October 20, 2017

Published online:

- [1] B. Dunn, H. Kamath, J.-M. Tarascon, *Science* **2011**, *334*, 928.
- [2] M. S. Whittingham, *Chem. Rev.* **2004**, *104*, 4271.
- [3] M. M. Thackeray, C. Wolverton, E. D. Isaacs, *Energy Environ. Sci.* **2012**, *5*, 7854
- [4] M. Pasta, C. D. Wessells, N. Liu, J. Nelson, M. T. McDowell, R. A. Huggins, M. F. Toney, Y. Cui, *Nat. Commun.* **2014**, *5*, 3007.
- [5] J. Liu, *Adv. Funct. Mater.* **2013**, *23*, 924.

- [6] L. Mai, X. Tian, X. Xu, L. Chang, L. Xu, *Chem. Rev.* **2014**, *114*, 11828.
- [7] H. Lee, M. Yanilmaz, O. Toprakci, K. Fu, X. Zhang, *Energy Environ. Sci.* **2014**, *7*, 3857.
- [8] D. Larcher, J.-M. Tarascon, *Nat. Chem.* **2015**, *7*, 19.
- [9] N. Yabuuchi, K. Kubota, M. Dahbi, S. Komaba, *Chem. Rev.* **2014**, *114*, 11636.
- [10] M. H. Han, E. Gonzalo, G. Singh, T. Rojo, *Energy Environ. Sci.* **2015**, *8*, 81.
- [11] Y.-K. Sun, Z. H. Chen, H.-J. Noh, D.-J. Lee, H.-G. Jung, Y. Ren, S. Wang, C. S. Yoon, S.-T. Myung, K. Amine, *Nat. Mater.* **2012**, *11*, 942.
- [12] H. Liu, Y. Wang, L. Li, K. Wang, E. Hosono, H. Zhou, *J. Mater. Chem.* **2009**, *19*, 7885.
- [13] C. J. Xu, B. H. Li, H. D. Du, F. Y. Kang, *Angew. Chem., Int. Ed.* **2012**, *51*, 933.
- [14] Y. Wang, J. Liu, B. Lee, R. Qiao, Z. Yang, S. Xu, X. Yu, L. Gu, Y. S. Hu, W. Yang, K. Kang, H. Li, X. Q. Yang, L. Chen, X. Huang, *Nat. Commun.* **2015**, *6*, 6401.
- [15] N. Zhang, F. Y. Cheng, Y.C. Liu, Q. Zhao, K. X. Lei, C. C. Chen, X. S. Liu, J. Chen, *J. Am. Chem. Soc.* **2016**, *138*, 12894.
- [16] M. H. Alfaruqi, V. Mathew, J. Gim, S. Kim, J. Song, J. P. Baboo, H. C. Sun, J. Kim, *Chem. Mater.* **2015**, *27*, 3609.
- [17] J. Lee, J. B. Ju, W. I. Cho, B. W. Cho, S. H. Oh, *Electrochim. Acta* **2013**, *112*, 138.
- [18] D. Xu, B. Li, C. Wei, Y.-B. He, H. Du, X. Chu, X. Qin, Q.-H. Yang, Y. F. Kang, *Electrochim. Acta* **2014**, *133*, 254.
- [19] B. J. Hertzberg, A. Huang, A. Hsieh, M. Chamoun, G. Davies, J. K. Seo, Z. Zhong, M. Croft, C. Erdonmez, Y. S. Meng, D. Steingart, *Chem. Mater.* **2016**, *28*, 4536.
- [20] H. L. Pan, Y. Y. Shao, P. F. Yan, Y. W. Cheng, K. S. Han, Z. M. Nie, C. M. Wang, J. H. Yang, X. L. Li, P. Bhattacharya, K. T. Mueller, J. Liu, *Nat. Energy* **2016**, *1*, 16039.
- [21] L. Y. Zhang, L. Chen, X. F. Zhou, Z. P. Liu, *Sci. Rep.* **2015**, *5*, 18263.
- [22] Z. Liu, G. Pulletikurthi, F. Endres, *ACS Appl. Mater. Interfaces* **2016**, *8*, 12158.
- [23] L. Y. Zhang, L. Chen, X. F. Zhou, Z. P. Liu, *Adv. Energy Mater.* **2015**, *5*, 1400930.
- [24] P. He, M. Y. Yan, G. B. Zhang, R. M. Sun, L. N. Chen, Q. Y. An, L. Q. Mai, *Adv. Energy Mater.* **2017**, *7*, 1601920.
- [25] D. Kundu, B. D Adams, V. Duffort, S. H. Vajargah, L. F. Nazar, *Nat. Energy* **2016**, *1*, 16119.
- [26] S. Liang, Y. Hu, Z. Nie, H. Huang, T. Chen, A. Pan, G. Cao, *Nano Energy* **2015**, *13*, 58.
- [27] T. Zhai, H. Liu, H. Li, X. Fang, M. Liao, L. Li, H. Zhou, Y. Koide, Y. Bando, D. Golberg, *Adv. Mater.* **2010**, *22*, 2547.
- [28] Y. Lu, J. Wu, J. Liu, M. Lei, S. Tang, P. Lu, L. Yang, H. Yang, Q. Yang, *ACS Appl. Mater. Interfaces* **2015**, *7*, 17433.
- [29] H. Wang, W. Wang, Y. Ren, K. Huang, S. Liu, *J. Power Sources* **2012**, *199*, 263.
- [30] C. Zhu, K. Song, P. A. van Aken, J. Maier, Y. Yu, *Nano Lett.* **2014**, *14*, 2175.
- [31] Z. V. Popovic, M. J. Konstantinovic, V. V. Moshchalkov, M. Isobe, Y. Ueda, *J. Phys.: Condens. Matter* **2003**, *15*, L139.
- [32] S. Franck, C. A. Kuntscher, I. Gregora, T. Yamauchi, Y. Ueda, *Phys. Rev. B: Condens. Matter Mater. Phys.* **2007**, *76*, 75128.
- [33] J.-K. Kim, B. Senthilkumar, S. H. Sahngong, J.-H. Kim, M. Chi, Y. Kim, *ACS Appl. Mater. Interfaces* **2015**, *7*, 7025.
- [34] M. H. Alfaruqi, V. Mathew, J. Song, S. Kim, S. Islam, D. T. Pham, J. Jo, S. Kim, J. P. Baboo, Z. Xiu, K. S. Lee, Y. K. Sun, J. Kim, *Chem. Mater.* **2017**, *29*, 1684.
- [35] P. Senguttuvan, S. D. Han, S. Kim, A. L. Lipson, S. Tepavcevic, T. T. Fister, I. D. Bloom, A. K. Burrell, C. S. Johnson, *Adv. Energy Mater.* **2016**, *6*, 1600826.
- [36] L. Mai, Y. Dong, L. Xu, C. Han, *Nano Lett.* **2010**, *10*, 4272.
- [37] W. Guoxiu, L. Hao, L. Jian, Q. Shizhang, L. G. Max, M. Paul, A. Hyojun, *Adv. Mater.* **2010**, *22*, 4944.
- [38] E. Brown, J. Acharya, G. P. Pandey, J. Wu, J. Li, *Adv. Mater. Interfaces* **2016**, *3*, 23.